NANO LETTERS

2009
Vol. 9, No. 11
3732-3738

# Acousto-plasmonic Hot Spots in Metallic Nano-Objects

**Nicolas Large,[†,‡] Lucien Saviot,[§] Jérémie Margueritat,[||,▽] José Gonzalo,[||] Carmen N. Afonso,[||] Arnaud Arbouet,[†] Pierre Langot,[⊥] Adnen Mlayah,[*,†] and Javier Aizpurua[*,‡,#]**

*Centre d'Elaboration des Materiaux et d'Etudes Structurales CEMES-CNRS, and Université de Toulouse, Toulouse, France, Centro Mixto de Física de Materiales CSIC-UPV/EHU and Donostia International Physics Center DIPC, San Sebastián, Spain, Institut Carnot de Bourgogne, UMR 5209 CNRS-Université de Bourgogne, Dijon, France, Laser Processing Group, Instituto de Óptica CSIC, Madrid, Spain, CPMOH, Université Bordeaux 1, Talence, France, and LCAM Laboratoire des Collisions Atomiques et Moléculaires, Université Paris Sud XI, Orsay, France*

*Received June 16, 2009; Revised Manuscript Received August 20, 2009*

**ABSTRACT**

**We investigate the acousto-plasmonic dynamics of metallic nano-objects by means of resonant Raman scattering and time-resolved femtosecond transient absorption. We observe an unexpectedly strong acoustic vibration band in the Raman scattering of silver nanocolumns, usually not found in isolated nano-objects. The frequency and the polarization of this unexpected Raman band allow us to assign it to breathing-like acoustic vibration modes. On the basis of full electromagnetic near-field calculations coupled to the elasticity theory, we introduce a new concept of "acousto-plasmonic hot spots" which arise here because of the indented shape of the nanocolumns. These hot spots combine both highly localized surface plasmons and strong shape deformation by the acoustic vibrations at specific sites of the nano-objects. We show that the coupling between breathing-like acoustic vibrations and surface plasmons at the "acousto-plasmonic hot spots" is strongly enhanced, turning almost silent vibration modes into efficient Raman scatterers.**

Metallic nano-objects sustain strongly localized surface charge density oscillations so-called surface plasmons. The use of these elementary excitations for generating, absorbing, guiding, and scattering the light has led to new technological applications in diverse scientific fields: strong local heating for cancer therapy,[1] squeezing of light into the nanoscale for high spatial resolution microscopy,[2] surface-enhanced Raman and infrared spectroscopies,[3,4] field-enhanced molecular fluorescence,[5] and nanobiosensing based on the surface plasmons resonances.[6,7] The electromagnetic near-field distribution associated with the excitation of localized surface plasmons has been extensively studied both theoretically and experimentally in static objects and nanostructures.[8−15] Only few experimental techniques address the dynamics of the surface plasmons of vibrating nano-objects. Among these techniques, resonant Raman scattering[16] and time-resolved transient absorption[17−21] are excellent methods to probe the coupling between surface plasmons and acoustic vibrations of metallic nano-objects. Both techniques provide complementary information as they involve the activation of different vibration modes.[18] In addition to the intrinsic interest in the fundamental understanding of the coupling mechanisms between the collective electronic and vibronic excitations, these noninvasive optical techniques are extremely useful in nanometrology (measurements of size and shape distributions).

In this Letter, we report on the role of localized surface plasmons of nano-objects in the anomalous activation of resonant Raman scattering by acoustic vibrations. The studied nano-objects consist of silver nanocolumns (NCls) grown by self-alignment of Ag spheroidal nanoparticles (NPs). All the nanocolumns are oriented in the same direction and intense localized surface plasmons (hot spots) arise because of the indentations along the nanocolumns. These peculiarities allow for the investigation of Raman selection rules and hence of the coupling between vibration modes with different

* To whom correspondence should be addressed: mlayah@cemes.fr and aizpurua@ehu.es.
[†] CEMES-CNRS, and Université de Toulouse, Toulouse.
[‡] CFM CSIC-UPV/EHU and DIPC, San Sebastián.
[§] Université de Bourgogne, Dijon.
[||] Instituto de Óptica CSIC, Madrid.
[⊥] CPMOH-Université Bordeaux 1, Talence.
[#] LCAM, Orsay.
[▽] Institut Carnot de Bourgogne, UMR 5209 CNRS-Université de Bourgogne, Dijon.

10.1021/nl901918a CCC: $40.75 © 2009 American Chemical Society
**Published on Web 09/09/2009**

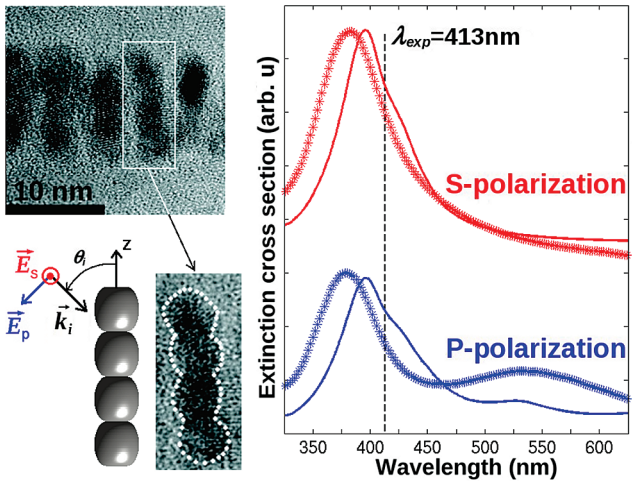


**Figure 1.** Left panel: TEM image cross section of the NCls and schematic of the incident light wavevector ($\vec{k}_i$) and electric fields for S- and P-polarizations. The angle between the incident wavevector and the NCl axis is $\theta_i = 34.5°$ inside the sample. A zoom of the TEM image shows a typical NCl formed by a stacking of quasi-spherical NPs. This stacking is modeled by an indented NCl as displayed in the schematics. Right panel: Calculated (full line) and measured (stars, sample NCls2) extinction spectra for P-polarized (blue) and S-polarized (red) light. The Raman excitation wavelength (413 nm) is marked on the graph as a dashed line.

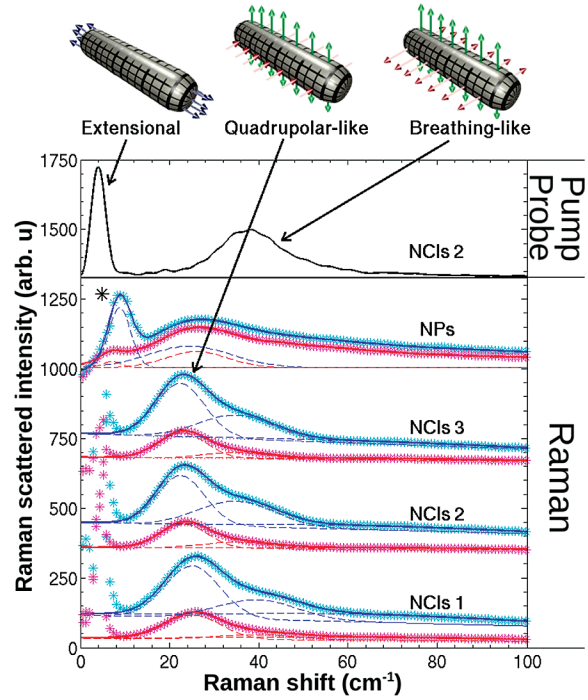


**Figure 2.** From bottom to top: Resonant Raman spectra (stars) of samples NCls1, NCls2, and NCls3 and of isolated nanoparticles (NPs) for P-polarized (blue) and S-polarized (red) incident light. The corresponding fits (full lines) have been obtained using two Gaussian line shapes and a background (dashed lines). Upper spectrum is the Fourier transform of the oscillating component of the time-resolved transient absorption from sample NCls2. Field displacement vectors of the vibrations are shown with the sketches in the upper part of the figure. The peak marked by a black star in the spectrum of the sample containing isolated nanoparticles corresponds to the Brillouin peak of the Si substrate.

symmetries and the surface plasmons excited at the nanocolumns. For the interpretation of our experiments we present fully integrated acousto-plasmonic calculations. The dynamical modulation of the surface plasmons by the acoustic vibrations is simulated using the boundary element method (BEM)[22,23] for the electromagnetic fields and the elasticity theory for the acoustic vibrations. We map the changes in the near-field around the vibrating nano-objects for the relevant acoustic modes which are anomalously observed in the Raman spectra. We introduce the concept of "acousto-plasmonic hot spots" as the sites in a nanostructure where an acoustic vibration produces large modulation of the localized near-field. The dynamics of the surface plasmons−acoustic vibrations interaction can be observed providing information on the coupling strength between the optically excited surface plasmons and the vibrations. We show how the presence of "acousto-plasmonic hot spots" at specific sites of the NCls are responsible for enhancement of the Raman scattering.

Ag:$Al_2O_3$ nanocomposite thin films containing Ag NCls were produced on glass substrates by alternate pulsed laser deposition (a-PLD)[16,17] of Ag nanoparticles and amorphous $Al_2O_3$ layers (a-$Al_2O_3$). When the thickness of the a-$Al_2O_3$ layers is reduced down to a critical value, Ag nanoparticles nucleate preferentially on top of nanoparticles of the previous layers, leading to the formation of self-aligned Ag NCls,[16] as observed in the TEM image in Figure 1. Three silver nanocolumn samples, with mean lengths of 6.5, 12, and 13 ± 0.2 nm (labeled NCls1, NCls2, and NCls3, respectively) and a mean diameter of 2.5 ± 0.2 nm, were studied. Optical extinction spectra from NCls2 were measured for both P and S incident polarizations. The experimental spectra in Figure 1 show a clearly defined transverse plasmon resonance (around 375 nm)[24] visible for P- and S-polarizations (see schematics of incident polarization in Figure 1), and a red-shifted broad band which has been already assigned to the longitudinal surface plasmon resonance[16] of the nanocolumns; the latter is only observed for P-polarization. The longitudinal-transverse surface plasmon splitting reveals the elongated nature of our nano-objects, consistent with the TEM images.

Low-frequency Raman scattering by confined acoustic vibrations was excited using the $\lambda_{exp} = 413$ nm krypton laser wavelength close to the transverse surface plasmon resonance (dashed line in Figure 1). The scattered light was dispersed using a customized T64000 Jobin-Yvon spectrometer which allows for low-frequency Raman−Brillouin measurements with a very high rejection of the Rayleigh scattering.

Figure 2 shows the Raman spectra recorded from the three NCls samples (NCls1, NCls2, NCls3) and from a sample consisting of five well-separated layers of isolated spherical nanoparticles (NPs) grown on a Si substrate. We use both P- and S-polarizations of the incident light, whereas the polarization of the scattered light is analyzed in the horizontal direction in the plane of incidence. This scattering configuration, together with the identical orientation of all the NCls allow for tracing the activation of different vibrational modes (selection rules) that could not be possible with randomly

oriented objects. The Raman scattering weakens and disappears when increasing the detuning between the wavelength of the laser and that of the surface resonances therefore we can conclude that surface plasmons are the most important intermediate states of the resonant Raman scattering process.

The Raman spectra of the NCls consist of a main peak located around 23 ± 2 $cm^{-1}$, which has been previously ascribed to scattering by quadrupolar-like confined acoustic vibration modes[16,17] (a sketch of the associated displacement field is shown in Figure 2). As observed in the spectra of NCls1, NCls2, and NCls3, the frequency of the quadrupolar-like Raman band is basically independent of the NCls length, with very small shifts due to differences in the lateral average dimensions of the nanocolumns. The extensional vibration mode of the NCls (shown in the sketch of Figure 2) can be observed only in time-resolved pump−probe experiments.[17] For that purpose, femtosecond time-resolved transient absorption measurements were performed using the pump−probe technique (excitation at 860 nm and detection at 430 nm).[17] Only the result obtained for NCls2 is presented here for comparison with the Raman data. The Fourier transform (FT) of the transient absorption oscillations from NCls2 (top spectrum of Figure 2) indeed exhibits a spectral line around 5 $cm^{-1}$. This line shifts down with increasing nanocolumn length as shown in ref 17. Moreover, a band around 38 ± 2 $cm^{-1}$, identified as a breathing-like mode of the nanocolumns, can also be observed in the FT spectrum (see sketch on the top of Figure 2).

In the Raman spectra, remarkably, an additional band is visible on the high frequency tail of the quadrupolar-like mode for the three nanocolumn samples (NCls1, NCls2, NCls3). This band is mainly observed for P-polarization (blue line) and almost vanishes for S-polarization (red line). The observation of this "anomalous" band in the Raman spectra is a striking finding. By fitting the Raman spectra with Gaussian line shapes, we extract the frequencies, bandwidths, and relative intensities of the observed bands. The Raman bandwidth is due to both homogeneous and inhomogeneous broadening of the vibration modes. The homogeneous broadening is due to the presence of a matrix and increases with decreasing NP size (ref 25). From our time-resolved pump−probe experiments (Figure 2) we estimate the homogeneous broadening of the breathing-like mode to be around $\Gamma_{hom} \approx 16$ $cm^{-1}$. On the other hand, the contribution of the NCls width distribution (0.4 nm) to the inhomogeneous broadening is estimated to be around $\Gamma_{inhom} \approx 4$ $cm^{-1}$. The homogeneous broadening and the inhomogeneous broadening due to the lateral size distribution of the NCls solely cannot fully explain the observed Raman bandwidth which is around 20 $cm^{-1}$. From the TEM image (Figure 1) one can notice that the NCls may strongly differ in shape (misalignment of the NP) as they consist of the stacking of 3−5 NPs. This shape distortion is responsible for an additional inhomogeneous broadening. This is the reason why Gaussian functions are used rather than Lorentzian for the fitting of the Raman spectra. The frequency of the "anomalous" band is dispersed from 39 $cm^{-1}$ (NCls1) to 36 $cm^{-1}$ (NCls2) and 35 ± 2 $cm^{-1}$ (NCls3) quasi-independently on the NCl length, similar to

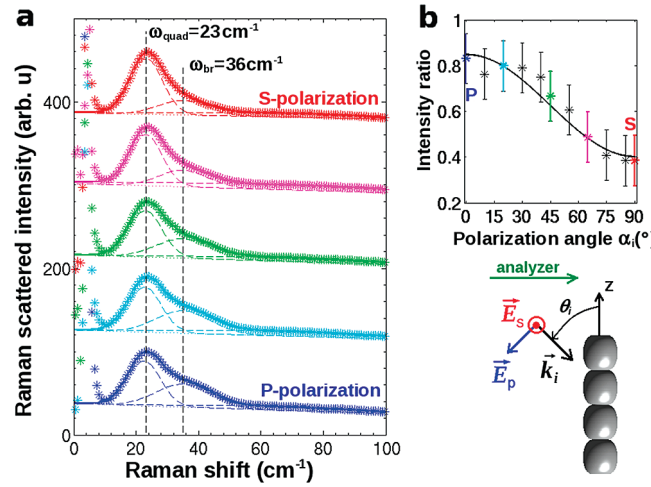


**Figure 3.** (a) Resonant Raman spectra (stars) from sample NCls2 and the corresponding fits (full lines) obtained with Gaussian line shapes (dashed lines), for six polarization angles from P (blue) to S (red) configurations. (b) Integrated intensity of the band at 36 $cm^{-1}$ normalized to that of the quadrupolar-like mode as a function of the polarization angle $\alpha_i$ (points) defined by $\vec{E}_i = \vec{E}_P \cos \alpha_i + \vec{E}_S \sin \alpha_i$. The green arrow indicates the direction onto which the scattered light is analyzed. The line is a fit to the experimental data obtained with 0.46 $\cos^2 \alpha_i$ + 0.4.

the behavior of the quadrupolar-like mode. Interestingly, the frequency of the anomalous band is very close to that of the breathing-like vibration band observed in the FT spectrum of the transient absorption. It seems natural to associate the additional band observed in the NCls Raman spectra to scattering by their breathing-like acoustic vibrations.

However, according to the surface orientation mechanism,[26,27] which has been shown to be the most important mechanism for the Raman scattering by acoustic vibrations in metallic nano-objects, breathing-like vibrations are not expected to have a strong Raman activity. Indeed, this mechanism involves the surface plasmon polarization field modulation by shape deformation of the nano-object (modulation of the surface polarization charges by the vibrations). Therefore, because breathing-like vibrations produce mainly a volume change and not a shape deformation, they are hardly observed by Raman scattering. Nevertheless the associated volume change gives rise to deformation potential interaction with the surface plasmons. For silver nano-objects this Raman scattering mechanism is about 1 order of magnitude less efficient than the surface orientation mechanism.[26,27] As a matter of fact, quadrupolar-like vibration modes dominate the Raman spectra (Figure 2) owing to the strong shape deformation they produce, thus leading to efficient modulation of the surface plasmon polarization.[26,27]

To further investigate the activation of the "anomalous" band, we trace the dependence of the Raman spectra on the two polarization components of the excitation light. Figure 3 shows the vanishing of this band when continuously changing the polarization from P to S. Figure 3b gives the variation of the integrated intensity of the "anomalous" band normalized to that of the quadrupolar-like vibration band. A clear cosine-like intensity evolution is observed.

For S-polarized incident light, the electric field is perpendicular to that of the scattered and analyzed light. In this crossed configuration, only acoustic vibrations projecting the polarization vector onto the perpendicular direction, because of shape deformation, are observable. This is the case of the quadrupolar-like vibrations, which are indeed observed in both crossed and parallel configurations (Figure 2). On the other hand, breathing-like vibrations do not present such a projection since they do not produce shape deformation of the vibrating object. As a consequence, Raman scattering by breathing-like modes, if activated, would occur only in the parallel configuration. This is precisely the tendency observed in Figures 2 and 3 for the "anomalous" band (significant intensity decrease in the crossed configuration). In comparison, the line shape of the Raman spectra recorded from isolated nanoparticles in both crossed and parallel configurations are identical (NPs in Figure 2) thus indicating the absence of any contribution from breathing vibrations. The scattering in this case is dominated by the well-known quadrupolar acoustic vibration modes allowed in both configurations.[28] All the above strongly support the assignment of the "anomalous" band to breathing-like acoustic vibrations of the NCls.

To address the reason why the breathing-like acoustic vibrations of the NCls efficiently scatter the light inelastically, we perform dynamical simulations of the surface plasmons near-field for these particular vibration modes. First, we calculate the acoustic vibration eigenmodes and then we use the associated displacement fields as geometrical boundary inputs for the calculation of the surface plasmons eigenstates. The modulation of the surface plasmons electromagnetic near-field generated in that way determine the Raman activity of the vibration modes.

We model the NCls using two different shapes: (i) smooth cylindrical nanocolumns and (ii) nanocolumns showing indentations (see sketch in Figure 1). The indented nanocolumn resembles more accurately the shape of the actual NCls as shown in Figure 1 due to the growth process (self-alignment of spherical NPs). Of course the exact shape may fluctuate and the indentations may be more or less pronounced depending on the NCls. Nevertheless, the theoretical results presented in this work and the interpretation of the experimental data do not depend critically on the exact NCls shape.

The vibrations of the NCls were calculated assuming an elastic continuous medium[29−32] and using the resonant ultrasound spectroscopy (RUS) method proposed by Visscher et al.[33,34] Because of the polycrystalline nature of the NCls, the mechanical properties of silver were approximated by isotropic elastic constants.[16] The nanocolumns are considered to be in vacuum.[35] The calculations provide both the eigenfrequencies and the eigenvectors of the vibrations. The irreducible representations as well as the volume variation, associated to each vibration mode can be determined in this way,[36] thus providing a straightforward way to identify the modes. In Figure 4 the surface displacement fields of our indented nanocolumn are shown for four relevant acoustic vibration modes: (a) extensional mode ($A_{1g}$ symmetry), (b) quadrupolar-like mode ($E_{2g}$ symmetry), (c) and (d) two breathing-like modes ($A_{1g}$ symmetry). The dynamics of the surface deformation associated with each vibration mode is provided as a video in the Supporting Information.

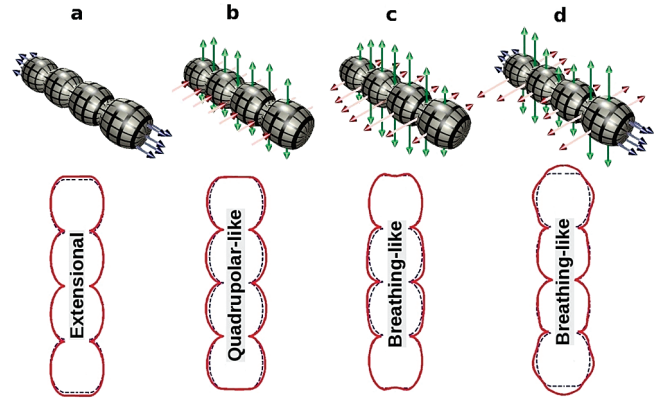


| | $\omega_{exp}$ (cm$^{-1}$) | | $\omega_{calc}$ (cm$^{-1}$) | |
|---|---|---|---|---|
| Extensional | 5 | (Pump-Probe) | (a) | 4 |
| Quadrupolar-like | 23 | (Raman) | (b) | 16 |
| Breathing-like | 36 | (Raman), | (c) | 34 |
| | 38 | (Pump-Probe) | (d) | 36 |

**Figure 4.** Relevant vibration modes of the indented nanocolumns. The arrows show the displacement eigenvectors at the surface of the model nanocolumn vibrating in its (a) extensional, (b) quadrupolar-like, (c) and (d) breathing-like eigenmodes. Cross section along the NCl main axis shows the deformed surface (red line) and the surface of the NCl at equilibrium (blue dashed line). The calculated $\omega_{calc}$ and measured $\omega_{exp}$ vibration frequencies are quoted in the table.

The vibration frequencies calculated for the extensional (a) and quadrupolar-like (b) modes are 4 and 16 cm$^{-1}$, respectively (see table in Figure 4), in good agreement with the band frequencies observed in time-resolved FT (5 cm$^{-1}$) and Raman spectra (23 ± 2 cm$^{-1}$). The two breathing-like modes (c and d in Figure 4) are radial modes mainly ($A_{1g}$ symmetry); they give rise to the largest volume variation. The fact that we obtain two breathing-like modes, and not a single mode as for an isolated spherical particle, can be understood in terms of mixing between the spheroidal vibration modes of a spherical particle when the shape evolves from a sphere to a column.[29] The two breathing-like modes (c) and (d) are quasi-degenerated: 34 cm$^{-1}$ for mode (c) and 36 cm$^{-1}$ for mode (d). Their average frequency is in excellent agreement with the frequency of the breathing-like vibration observed in the FT spectrum (Figure 2) of the time-resolved transient absorption oscillations. More interestingly the agreement with the frequency of the "anomalous" Raman band is remarkable.[35] This provides additional support for the assignment of the "anomalous" Raman band to scattering by breathing-like acoustic vibrations.

We address now the optical response and the acousto-plasmonic dynamics of the nanocolumns. Using the BEM, we solve exactly Maxwell's equations for the experimental excitation conditions and for both static and vibrating nanocolumns. The calculated extinction spectra are shown in Figure 1. The transverse plasmon resonance is well reproduced by the simulations. However, a small shift

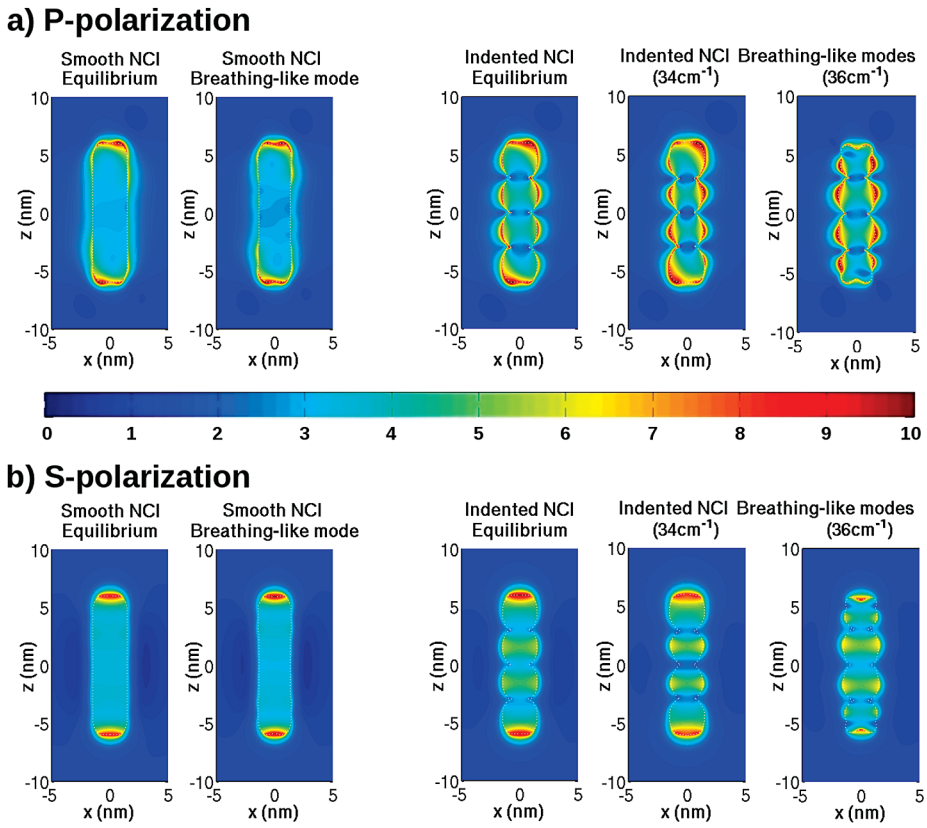


**Figure 5.** Electric field distribution around the smooth cylindrical and indented nanocolumns calculated for the experimental configuration at $\lambda_{exp} = 413$ nm and for both P- and S-polarizations (respectively a and b). The color scale corresponds to the field enhancement factor $(|E(\vec{r})|)/(|E_i(\vec{r})|)$.

(around 15 nm) between the calculated and the measured resonances can be noticed. This shift is due to interactions between the NCls not taken into account in our simulations. Nevertheless, in our case, the characteristics of incidence direction and wavelength of the incoming light excite basically transverse excitations where the effect of interparticle interaction is reduced,[37,38] with high localization of the near field at each single particle.[39] Additionally, the presence of the indentations further localizes the near field, making the response of the individual nanocolumns the main responsible for the modulation of the near field.

In metallic nano-objects, surface plasmons play the role of the intermediate electronic states in the resonant Raman scattering. The scattering process can be described as a three-step process:[26] absorption of the incident photon, absorption or emission of a vibration mode, and emission of the scattered photon

$$\left|\sum_{a,b}\left[\langle n_{\vec{k}_s}^{-}+1, n_b|H^{s}_{pl-phl}|n_{\vec{k}_s}^{-}, n_b+1\rangle\langle n_b+1, n_a|H_{\text{pl-vib}}|n_b, n_a+1\rangle\langle n_{\vec{k}_i}^{-}, n_a+1|H^{i}_{\text{pl-pht}}|n_{\vec{k}_i}^{-}+1, n_a\rangle\right/\left[(\hbar\omega_s-\hbar\omega_b+i\Gamma_b)(\hbar\omega_i-\hbar\omega_a+i\Gamma_a)\right]\right|^2 \quad (1)$$

where $n_{\vec{k}_{i(s)}}^{-}$ is the number of incident (respectively scattered) photons with wavevector $\vec{k}_{i(s)}$ and energy $\hbar\omega_{i(s)}$. $n_{a(b)}$, $\hbar\omega_{a(b)}$, and $\Gamma_{a(b)}$ are the occupation numbers, energy, and homogeneous broadening of the intermediate surface plasmon states (labeled $a$ and $b$) involved in the optical absorption and emission steps. $H^{i(s)}_{\text{pl-pht}}$ is the interaction Hamiltonian between the surface plasmons and the incident (respectively scattered) light. The acoustoplasmon interaction considered here is due to the surface orientation mechanism given by[26]

$$\langle n_b+1, n_a|H_{\text{pl-vib}}|n_b, n_a+1\rangle = -\int_{\text{NCl}}\vec{E}_b(\vec{r})\cdot\delta_{\text{vib}}\vec{P}_a(\vec{r})\,\mathrm{d}V \quad (2)$$

where $\delta_{\text{vib}}\vec{P}_a(\vec{r})$ is the modulation of the optically excited polarization by the acoustic vibrations and $\vec{E}_b(\vec{r})$ is the electric field of the surface plasmon state emitting the scattered photon. The integral runs over the entire volume.

Because the acousto-plasmonic interaction depends on the modulation of the polarization associated to a particular vibration mode, we calculate now the evolution of the near-field distribution for the relevant breathing-like modes (video in Supporting Information). All the simulations are performed at the experimental excitation wavelength, polarization (both P and S), and angle of incidence. We provide snapshots of the NCls at equilibrium and at maximum deformation in Figure 5. In terms of interaction steps, this is equivalent to map the first two steps in the resonant Raman process described by eq 1: optical excitation of the surface plasmon (first intermediate state) and subsequent interaction with the vibration mode given by eq 2.

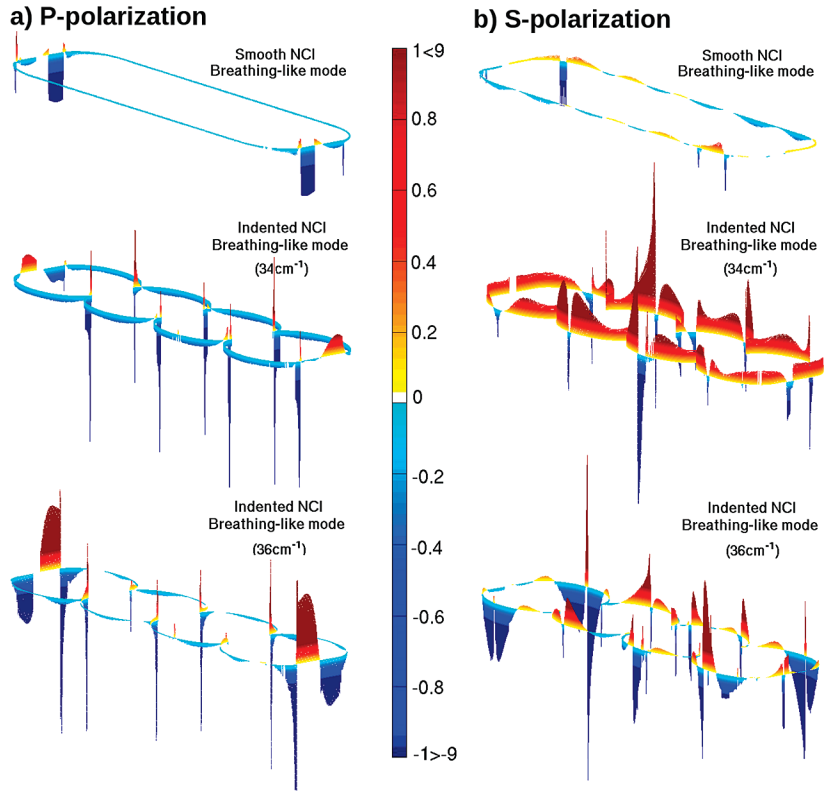


**Figure 6.** Relative modulation of the amplitude of the induced polarization by the breathing-like modes at a fixed distance of 0.5 nm from the NCls surface at rest ($\delta_{vib}|\vec{P}|/|\vec{P}_0|$). The modulation, shown here for the smooth and indented nanocolumns, were calculated for the experimental configuration at $\lambda_{exp} = 413$ nm, an incidence angle $\theta_i = 34.5°$, and for both P- and S-polarizations (a and b, respectively). The color scale saturates at $-1$ and 1 even though the minimum and the maximum values are $-9$ and 9, respectively.

When we describe our nano-objects as smooth cylindrical NCls, i.e., without indentations (left panels in Figure 5), the modulation of the surface plasmon near-field by the breathing-like vibrations is very weak for both P (a) and S (b) polarized light. In contrast, for the indented NCls, the surface plasmon near-field is strongly modulated by the breathing-like vibration modes (right panels in Figure 5). Modulation occurs for both P- and S-polarizations (see Figure 3). The strong surface plasmon modulation is due to (i) the near field intensity accumulation in the regions of indentations and (ii) the strong local shape deformation by the acoustic displacement also mediated by the presence of indentations (see Figure 4 and Supporting Information). Following the dependence of the vibration−plasmon coupling strength from eq 2, both effects (i and ii) enhance the modulation of the surface plasmon polarization $\delta_{vib}\vec{P}_a$ and effectively activate the Raman scattering by the breathing-like vibration modes.

In order to gain more insight in the understanding of the role of the NCls shape, we finally present a quantitative analysis of the acousto-plasmonic dynamics. Figure 6 shows the spatial distribution of the relative modulations ($\delta_{vib}|\vec{P}|/|\vec{P}_0|$) of the surface plasmon polarization by the breathing-like modes (see Figure 4 and Supporting Information) for both smooth and indented NCls; $\vec{P}_0$ and $\delta_{vib}|\vec{P}|$ (see eq 2) are respectively the surface plasmons polarization and the modulation of its amplitude both calculated at a fixed distance of 0.5 nm from the NCls surface (at rest). The surface plasmon polarization modulation is once again much larger for the indented NCls than for the smooth cylindrical NCls, particularly around the regions of indentations. The spikes in $\delta_{vib}|\vec{P}|/|\vec{P}_0|$ arising from the strong shape deformation at the indentations can be considered as the hot spots of the acousto-plasmonic interaction. For P-polarized light (left panels in Figure 6), the relative modulation $\delta_{vib}|\vec{P}|/|\vec{P}_0|$ ranges from $-9$ to 4 for the breathing-like mode at 34 $cm^{-1}$, and from $-9$ to 6 for the mode at 36 $cm^{-1}$, depending on the considered point. For the smooth NCls, the maximum and minimum of $\delta_{vib}|\vec{P}|/|\vec{P}_0|$ are $-4$ and 2, respectively, and are visible only around the NCls end regions, whereas along the NCl walls $\delta_{vib}|\vec{P}|/|\vec{P}_0|$ presents a very small value not exceeding $-0.05$. Similarly, with S-polarized light (right panels in Figure 6), the relative modulation $\delta_{vib}|\vec{P}|/|\vec{P}_0|$ ranges from $-9$ to 9 for both breathing-like modes of the indented NCls and is larger than that calculated for the smooth NCls. As can be noticed in Figure 5 and Figure 6, the modulation of the surface plasmons occurs for both P- and S-polarized incident light whereas the Raman scattering by breathing-like vibrations appears mainly for P-polarization (Figure 3 and Figure 4). The reason lies in the fact that the Raman process does not consist only of the optical excitation of the surface plasmons and their modulation by the vibrations but also of the emission of the scattered photon (outgoing photon term in eq 1). Indeed, the extinction of the Raman scattering for S-polarization is due to the fact that the scattered light is analyzed in the orthogonal direction (crossed configuration). In other words, even though the surface plasmons are efficiently excited with S-polarized incident light and strongly modulated by the breathing-like vibrations, the corresponding

$\delta_{vib}\vec{P}_a$ (eq 2) has no component on the direction perpendicular to $\vec{P}_a$ because of the shape conserving deformation.

The modulation of the optically induced polarization gives the strength of the acoustoplasmons coupling. Indeed, the acousto-plasmonic hot spots (spikes visible in Figure 6 for the indented NCls) give rise to nonvanishing interaction matrix elements (eq 2), thus leading to the activation of breathing-like vibration modes which are otherwise inefficient Raman scatterers. In fact, considering the wall region of the indented NCls, the relative surface plasmons modulation is roughly in the range of 10 (between spikes) to 200 (at the spikes) times larger than that of the smooth NCls, depending on the considered point.

In conclusion, based on the concept of acousto-plasmonic hot spots, supported by numerical simulations, we provided a conceptual understanding of the fundamental mechanism leading to the activation of normally very weak vibration modes in the Raman scattering of nano-objects. We have shown that for the surface orientation mechanism, the breathing-like vibrations which are almost silent for smooth cylindrical nanocolumns are strongly enhanced in the case of indented nanocolumns. The indentations of the silver nanocolumns are responsible for the strong localization of the surface plasmon near field and its modulation by breathing-like acoustic vibrations. Understanding the acousto-plasmonic dynamics of metallic nano-objects is useful not only for the interpretation of Raman and time-resolved pump−probe experiments but also for nanometrology, i.e., extracting information on sizes and shapes distributions from these optical measurements. The concepts and the numerical and experimental approaches developed in this work are not specific to indented nanocolumns. They can be extended to other isolated nano-objects exhibiting strong field localization (because of their shape), to dimers of nano-objects (because of strong interaction in the gap region), and to more complex metallic nanostructures combining size, shape, and interaction effects.

**Acknowledgment.** This work was partially supported by C'Nano GSO program (France), by MAT2009-14282-C02-01, MCINN (Spain), by Spanish CSIC intramural project 200860I039, and by an "Integrated Action" between France and Spain (HF2008-0038).

**Supporting Information Available:** A video showing the time evolution of the surface displacement field for the (a) extensional, (b) quadrupolar-like, and (c) and (d) breathing-like vibration eigenmodes for both indented (lower part) and smooth cylindrical (upper part) nanocolumns. For the indented NCls this corresponds to the dynamical view of Figure 4. The second video shows the acousto-plasmonic dynamics: time dependence of the surface plasmon near-field due to modulation by the breathing-like acoustic vibration modes for both smooth (left panels) and indented (right panels) nanocolumns. Simulations are presented for both P- and S-polarizations of the incident light and for the experimental configuration ($\lambda_{exp} = 413$ nm, incidence angle $\theta_i = 34.5°$). Snapshots of this dynamical view are shown in Figure 5. This material is available free of charge via the Internet at http://pubs.acs.org.

## References

(1) Lal, S.; Clare, S. E.; Halas, N. J. *Acc. Chem. Res.* **2008**, *41*, 1842–1851.
(2) Hillenbrand, R.; Keilmann, F.; Hanarp, P.; Sutherland, D. S.; Aizpurua, J. *Appl. Phys. Lett.* **2003**, *83*, 368–370.
(3) Xu, H.; Bjerneld, E. J.; Käll, M.; Börjesson, L. *Phys. Rev. Lett.* **1999**, *83*, 4357.
(4) Neubrech, F.; Pucci, A.; Cornelius, T. W.; Karim, S.; Garcia-Etxarri, A.; Aizpurua, J. *Phys. Rev. Lett.* **2008**, *101*, 157403.
(5) Kuhn, S.; Hakanson, U.; Rogobete, L.; Sandoghdar, V. *Phys. Rev. Lett.* **2006**, *97*, 017402.
(6) Dahlin, A.; Zäch, M.; Rindzevicius, T.; Käll, M.; Sutherland, D. S.; Höök, F. *J. Am. Chem. Soc.* **2005**, *127*, 5043–5048.
(7) Haes, A. J.; Van Duyne, R. P. *J. Am. Chem. Soc.* **2002**, *124*, 10596–10604.
(8) Xu, H.; Aizpurua, J.; Käll, M.; Apell, P. *Phys. Rev. E* **2000**, *62*, 4318.
(9) Nordlander, P.; Oubre, C.; Prodan, E.; Li, K.; Stockman, M. I. *Nano Lett.* **2004**, *4*, 899.
(10) Talley, C. E.; Jackson, J. B.; Oubre, C.; Grady, N. K.; Hollars, C. W.; Lane, S. M.; Huser, T. R.; Nordlander, P.; Halas, N. *Nano Lett.* **2005**, *5*, 1569.
(11) Aizpurua, J.; Bryant, G. W.; Richter, L. J.; García de Abajo, F. J.; Kelley, B. K.; Mallouk, T. *Phys. Rev. B* **2005**, *71*, 235420.
(12) Romero, I.; Aizpurua, J.; Bryant, G. W.; de Abajo, F. J. G. *Opt. Express* **2006**, *14*, 9988.
(13) Novotny, L.; Hecht, B. *Principles of Nano-Optics*; Cambridge University Press: Cambridge, 2007.
(14) Ringler, R. M.; Klar, T. A.; Schwemer, A.; Susha, A. S.; Stehr, J.; Raschke, G.; Funk, S.; Borowski, M.; Nichtl, A.; Kürzinger, K.; Phillips, R. T.; Feldmann, J. *Nano Lett.* **2007**, *7*, 2753.
(15) Le Ru, E. C.; Grand, J.; Félidj, N.; Aubard, J.; Lévi, G.; Hohenau, A.; Krenn, J. R.; Blackie, E.; Etchegoin, P. *J. Phys. Chem. C* **2008**, *112*, 8117.
(16) Margueritat, J.; Gonzalo, J.; Afonso, C. N.; Mlayah, A.; Murray, D. B.; Saviot, L. *Nano Lett.* **2006**, *6*, 2037–2042.
(17) Burgin, J.; Langot, P.; Arbouet, A.; Margueritat, J.; Gonzalo, J.; Afonso, C. N.; Vallée, F.; Mlayah, A.; Rossell, M. D.; Tendeloo, G. V. *Nano Lett.* **2008**, *8*, 1296–1302.
(18) Ikezawa, M.; Okuno, T.; Masumoto, Y. *Phys. Rev. B* **2001**, *64*, 201315(R).
(19) Nelet, A.; Crut, A.; Arbouet, A.; Del Fatti, N.; Vallée, F.; Portales, H.; Saviot, L.; Duval, E. *Appl. Surf. Sci.* **2004**, *226*, 209–215.
(20) Hartland, G. V. *Annu. Rev. Phys. Chem.* **2006**, *57*, 403–30.
(21) Zijlstra, P.; Tchebotareva, A. L.; Chon, J. W. M.; Gu, M.; Orrit, M. *Nano Lett.* **2008**, *8*, 3493–3497.
(22) García de Abajo, F. J.; Howie, A. *Phys. Rev. Lett.* **1998**, *80*, 5180–5183.
(23) García de Abajo, F. J.; Howie, A. *Phys. Rev. B* **2002**, *65*, 115418.
(24) Link, S.; Mohamed, M. B.; El-Sayed, M. A. *J. Phys. Chem. B* **1999**, *103*, 3073–3077.
(25) Del Fatti, N.; Voisin, C.; Chevy, C.; Vallée, C.; Flytzanis, F. *J. Chem. Phys.* **1999**, *110*, 11484.
(26) Bachelier, G.; Mlayah, A. *Phys. Rev. B* **2004**, *69*, 205408.
(27) Bachelier, G.; Margueritat, J.; Mlayah, A.; Gonzalo, J.; Afonso, C. N. *Phys. Rev. B* **2007**, *76*, 235419.
(28) Duval, E. *Phys. Rev. B* **1992**, *46*, 5795.
(29) Cheng, W.; Ren, S.-F.; Yu, P. Y. *Phys. Rev. B* **2005**, *71*, 174305.
(30) Cheng, W.; Ren, S.-F.; Yu, P. Y. *Phys. Rev. B* **2005**, *72*, 059901(E).
(31) Combe, N.; Huntzinger, J. R.; Mlayah, A. *Phys. Rev. B* **2007**, *76*, 205425.
(32) Ramirez, F.; Heyliger, P. R.; Rappé, A. K.; Leisure, R. G. *J. Acoust. Soc. Am.* **2008**, *123*, 709.
(33) Visscher, W. M.; Migliori, A.; Bell, T. M.; Reinert, R. A. *J. Acoust. Soc. Am.* **1991**, *90*, 2154.
(34) The displacement vectors are expanded onto an $x^i y^j z^k$ basis. We used $0 \le i + j + k \le 20$ in order to achieve a good numerical convergence.
(35) For comparison with the measured vibration frequencies the calculated values must be shifted upward by $2-3$ cm$^{-1}$ in order to take into account the matrix effect.[16]
(36) Saviot, L.; Murray, D. B. *Phys. Rev. B* **2009**, *79*, 214101.
(37) Kottmann, J.; Martin, O. *Opt. Express* **2001**, *8*, 655–663.
(38) Jain, P. K.; Eustis, S.; El-Sayed, M. A. *J. Phys. Chem. B* **2006**, *110*, 18243–18253.
(39) Ono, A.; Kato, J.; Kawata, S. *Phys. Rev. Lett.* **2005**, *95*, 267407.

NL901918A